SIMULATION OF A-SI PIN SOLAR CELLS WITH BUFFER

PFLEIDERER H.
Siemens Corporate Research, Otto-Hahn-Ring 6, 8000 München 83, Germany

ABSTRACT

The buffer of standard solar cells restricts the "surface recombination" at the front side. Some typical cell properties linked to the buffer are exposed by numerical simulations: The "blue snake" appearing in small-signal photocharacteristics, the electron inversion layer, the reverse field peak and the satellite space-charge dipole layer. It is possible to base a simulation on the roots of an algebraic equation.

INTRODUCTION

The p-layer of amorphous-silicon (a-Si) solar cells is doped with carbon (C) in order to widen the band gap and to better exploit the blue part of the sun spectrum [1]. The p(C)-i heterojunction involves an electron-affinity variation that can contribute to the achievable open-circuit voltage [2] and hinders electrons from the i-layer to recombine with holes from the p-layer [3]. A defective junction will again promote this kind of "surface recombination", however. Now the p-layer is certainly defective, and its boundary, the p-i junction, likewise [4]. Hence only a spatial separation of p-i junction and electron-affinity junction will secure a low surface-recombination loss of photocarriers [5]. Interposed between the p-i junction and the affinity barrier then is a C-rich but otherwise undoped layer called "buffer". It may consist of a uniform section with constant C-content and a graded section with gradients of C, band gap and electron affinity.The introduction of suitable buffers has led to an elevation of the open-circuit voltage. But under prolonged illumination preferentially the buffer degrades [6]. The present contribution is restricted to phenomenological considerations. The affinity gradient of a heterojunction disturbs the local space charges and recombination rates. A buffer exposes the typical traits most distinctly. An indication of them will be given.

PHYSICAL ASSUMPTIONS

The numerical simulations to be presented rest on a simple physical model. It uses a density-of-states distribution through the mobility gap consisting of 4 branches $D_i(E)$, i = 1 to 4, all of them exponential functions of the gap energy E [7]. The branches D_1 and D_2 (D_3 and D_4) represent donor-like tail and bottom states (acceptor-like bottom and tail states). The valence (conduction) band edge is $E = E_V = E_0 = 0$ ($E = E_C = E_4$). The branches intersect at $E_1 = 0.3$, $E_2 = 0.55$ and $E_3 = 0.8$ in units of the band gap $E_g = E_4$. The pin structure consists of 7 regions as sketched in Fig. 1. The regions 1 and 7 represent the p- and n-layers, regions 2 and 3 the buffer, and regions 4, 5 and 6 the i-layer. The band gap is $E_g = 2.0$ eV (1.7 eV) in regions 1,2 (4 to 7), and varies linearly through region 3. The density of states D_j assumes the values D_{ij} in the different regions j. Table I gives the width of the regions together with the values $D_{2j}(E_2) = D_{3j}(E_2)$ at the intersection between the bottom branches. The densities assumed at the band edges are $D_{1j}(E_0) = D_{4j}(E_4) = 10^{21}/cm^3$ eV independent of j, the densities at the intersection of the donor-like branches are $D_{1j}(E_1) = D_{2j}(E_1) = 10 \cdot D_{2j}(E_2)$, and the densities at the intersection of the acceptor-like states are

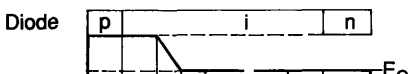

Fig.1 : Assumed cell structure

Table I : Regions j, widths and mid-gap densities of state $D_{2j}(E_2)$

	Region	1	2	3	4	5	6	7
Width	nm	15	15	10	10	415	15	20
$D_{2j}(E_2)$	$1/eVcm^3$	$2\cdot10^{18}$	$5\cdot10^{16}$	$1\cdot10^{17}$	$2\cdot10^{16}$	$5\cdot10^{15}$	$1\cdot10^{17}$	$2\cdot10^{18}$

$D_{3j}(E_3) = D_{4j}(E_3) = 5\cdot D_{3j}(E_2)$. Thus the functions $D_{ij}(E)$ are completely defined. The buffer is assumed to consist of section I with uniform band gap (region 2) and section II with graded band gap (region 3). The density of states is highest in the doped layers (regions 1 and 7), lowest in the central part of the i-layer (region 5), elevated in the outer parts of the i-layer (regions 4 and 6), and elevated also in the graded buffer section II (region 3).

The recombination traffic via a gap state depends on its capture cross section σ. A state can be neutral or charged. The ratio $\sigma(\text{charged})/\sigma(\text{neutral}) = 100$ will be used throughout. The capture coefficient $S = v_t\sigma(\text{neutral})$, with thermal velocity v_t, shall not depend on the gap energy, but can differ between the regions j. We put $S_j = 10^{m_j}\cdot10^{-10}\ cm^3/s$ with numbers m_j, choose $m_I = m_7 = 2$ and attribute m_I, m_{II} and m_{III} to the corresponding sections of Fig.1. Simulations will be presented of 3 cells differing only in the triple "$m_I m_{II} m_{III}$" assigned to them, namely "000", "030", and "002". The first cell serves as a fairly good reference, the second has a bad graded buffer section, and the third a bad i-layer. The uniform buffer section remains unaltered. The second and third cells represent examples for enhanced surface and bulk recombination, respectively. The introduction of a (heterojunction with) buffer diminishes surface recombination. In order to expose the influence of an electron affinity gradient we simply omit the band-gap gradient through region 3 and leave all other cell parameters untouched. The broken line in Fig.1 indicates the structure obtained in this way and the respective "virtual cells" are designated as 000*, 030*, and 002*.

Other cell parameters are relative permittivity $\varepsilon_r = 12$, intrinsic concentration (without C) $n_{i0} = 6\cdot10^5/cm^3$, mobilities of electrons $\mu_n = 10$ and of holes $\mu_p = 1\ cm^2/Vs$, doping potentials of the n- and p-layers $\psi_0(p) = -0.45$ and $\psi_0(n) = 0.5$ V relative to $E = E_2$, built-in voltage $U_b = \psi_0(n) - \psi_0(p) = 0.95$ V. The outer boundaries of the pin structure are $x = x_0$ (left side of region 1) and $x = x_7$ (right side of region 7). As boundary condition for the potential $\psi(x)$ under an applied voltage U the relation $\psi(x_7) - \psi(x_0) = U_b - U$ is used. The generation rate of photoelectrons due to AM1 illumination is derived from a simple optical model. It uses measured absorption constants as a function of the light wavelength λ, the transmission factor $T = 0.9$ to the front side $x = x_0$, and a reflection factor $R = 0.2$ at the back side $x = x_7$, these T- and R-values for any λ. The recombination rate of excess carriers and the space charge are controlled by the free electron and hole concentrations and depend on the gap states [8].

CHARACTERISTICS

The "apparent" properties of the simulated cell set are collected in Table II. It shows efficiency η, short-circuit current j_{sc}, fill factor ff, open-circuit voltage U_{oc} and diode quality factor n_Q. Only the qualitative trend counts. The modest η of the reference cell 000 stems from the rather low j_{sc}-value. The limitation of j_{sc} is due to the optical model that considers a flat pin structure. The cells 030 with degraded buffer and 000* without buffer are examples for enhanced surface recombination and cell 002 with degraded i-layer is an example for enhanced bulk recombination. We look for the dark current j_D at first. An increase of surface (bulk) recombination lowers (rises) the factor n_Q of the forward current while the reverse current, not shown in Table II, remains unaltered (rises also). So the enhancement of surface or bulk recombination exhibits different trends. A closer look reveals that n_Q depends on voltage U. While $n_Q(U)$ is constant for cell 000, it rises in case of cell 002 and falls for cells 030 and 000*. Table II shows average values of n_Q therefore.

Table II : Simulated cell properties

	Cell	000	030	002	000*	030*	002*
η	%	8.5	5.9	4.5	6.9	4.9	4.1
j_{sc}	mA/cm^2	13.7	11.9	11.7	13.3	10.6	11.3
ff	%	68	61	47	65	60	47
U_{oc}	V	0.91	0.80	0.81	0.81	0.76	0.76
n_Q		1.55	1.20	1.59	1.28	1.21	1.60

The light current j helps to define the photocurrent $j_P = j - j_D$. It tends under reverse voltage to a saturation value j_S. An internal collection efficiency is

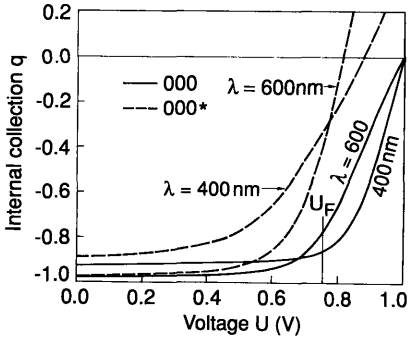

Fig.2 : q(U) for 2 cells

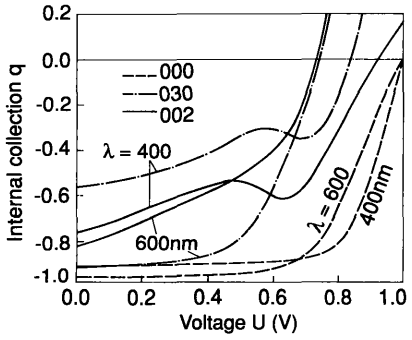

Fig.3 : q(U) for 3 cells

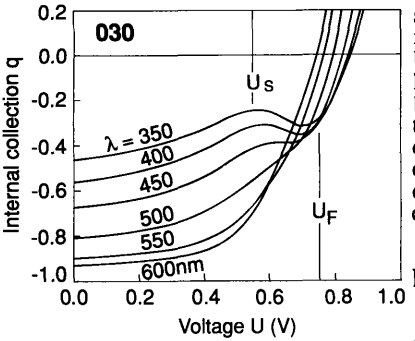

Fig.4 : q(U) for 1 cell

$q = -j_P/j_S$. Perfect collection is given with q=-1. The efficiency q and the photocurrent j_P have the same sign. It is q<0 (q>0) for primary (secondary) photocurrents. The following simulations are based on the auxilary definition $q = j_P/eG_i$ (with elementary charge e and generation rate G_i integrated through the i-layer) that circumvents j_S. The efficiencies calculated in this way are correct if the p- and n-layers are "dead". In order to achieve this the high capture coefficient $S = 10^{-8}cm^3/s$ is assumed for these layers.This measure also limits the j_{SC}- values of Table II. TheFig.2 gives plots of functions q(U) simulated with weak spectral light of two wavelengths λ (photon flux at $x = x_0$ is $F = 10^{12}/cm^2s$) for cells 000 and 000*. The curves for blue light (λ = 400 nm) and for red light (λ = 600 nm) cross near the flat-band voltage $U = U_F = 0.75$ V. At this voltage the electric field just vanishes in region 3 (as can be seen later on). The "cross efficiency" q_P is lower in absolute value without the affinity gradient. It is indeed already known from analytical [9] and numerical [10] simulations that enhanced surface recombination diminishes q_P. In Fig.3 the q(U) curves of the 3 heterocells are compared. Enhanced bulk recombination (cell 002) yields also a low value of q_P as enhanced surface recombination (cell 030). But the short-circuit q(0) spread between blue and red light is broad (narrow) for enhanced surface (bulk) recombination. The omission of the affinity gradient yields worse characteristics in any case and eliminates the slope reversal of the "blue characteristics" below the crossing of the bad cells. An indication of this "blue-snake phenomenon" is also apparant experimentally [9]. The affinity gradient in region 3 and notwithstanding strong recombination within the region (cell 030) or besides it (cell 002) are the preconditions for the appearance of "blue snakes" [11], and weak illumination. Fig.4 shows q(U) curves for cell 030 due to several λ. The blue snake crooks between voltages U_S and U_F. With forward voltages U rising above the threshold U_S the blue q(U) curves bend down. This behavior indicates diminishing surface recombination with growing U against the general trend. The field reversal at U_F launches abundant surface recombination, bends all q(U) curves up, and causes the transition between the diode and double-injection regimes of the dark characteristic.

Internal Properties

The following illustrations will be restricted to cell 030. The main attention will be paid to aspects brought in by the affinity gradient of

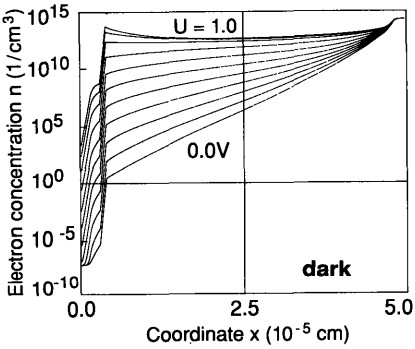

Fig.5 : n(x) through pin structure

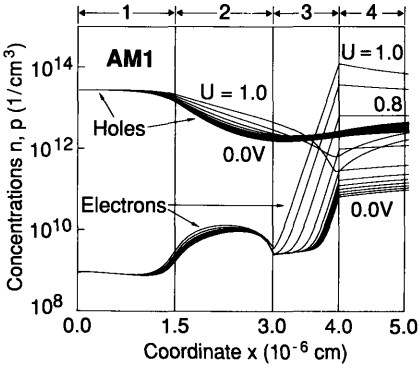

Fig.6 : n(x) and p(x) through 1 to 4

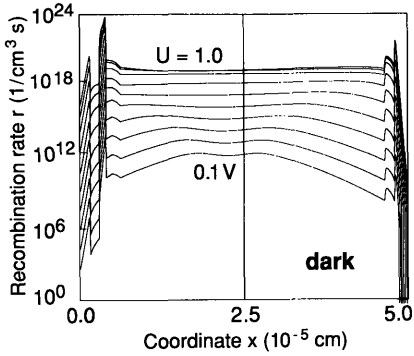

Fig.7 : r(x) through pin structure

region 3. Most indicative for the internal state of a cell is the carrier distribution through the pin structure. Fig.5 shows the electron concentration n versus coordinate x in the dark for voltages U=0 to 1.0 V in steps of 0.1 V. An AM1 illumination increases n(x) considerably, especially for the lower voltages. The functions n(x) through the front regions 1 to 4 alone under AM1 are depicted in Fig.6 together with the hole concentration p(x). The function n(x) rises sharply through region 3. For $U > U_F$ the concentration n(x) surpasses p(x) in region 4 and thus forms an inversion layer (also in the dark). The reversed field drives the electrons against the buffer barrier and piles them up. (Cell 030* shows no inversion layer.) The function p(x) dips down at the region boundary 3,4 for $U > U_F$ while the recombination rate r(x) becomes quite large there. The function r(x), Fig.7 shows it in the dark, has peaks near the p-i and i-n junction (surface recombination) and is rather constant in between (bulk recombination). In crossing the boundary 3,4 the function r(x) jumps down as does the capture coefficient S. (The reverse situation is given with cell 002.) All the regions of Fig.1 are recognizable in Fig.7. The rate r and the field $E = -\psi'$ are interdependent. Fig. 8 gives the potential gradient $\psi'(x)$ in the dark. The peaks mark the p-i and i-n junctions (the region boundaries 1,2 and 6,7). The field reverses its direction first in region 3 at $U = U_F$ and a "reverse peak" develops with $U > U_F$ that is linked to the affinity gradient and to the electron inversion layer. (Cell 030* shows no reverse peak.) AM1 light changes the field picture but not essentially. Figs.9 and 10 show the second derivatives $\psi''(x)$ through regions 1 to 4 and through region 3 alone. The sign reversal at the boundary 1,2 establishes a space-charge double layer associated to the left field peak of Fig.8. A satellite dipole layer evolves for $U > U_F$ in region 3 that corresponds to the reverse peak of Fig.8. With increasing voltage U the function $\psi''(x)$ decreases slowly in region 3 up to the threshold $U=U_S = 0.55V$ and rises quickly with $U > U_S$. This turn-up is linked to the blue snake of Fig.4 that expands between U_S and U_F. The typical internal aspects caused by the affinity gradient in region 3 - electron inversion, reverse field peak, satellite dipole layer - are all linked to each other. The high recombination rate in region 3 of cell 030 actually damps the build-up of an inversion layer. Hence cells 002 and 000 exhibit even stronger inversion layers. The above aspects, demonstrated here on the basis of quite special assumptions, should be of general significance. Another problem is to find and realize an effective buffer [12] that is hardened against degradation. The omission of the

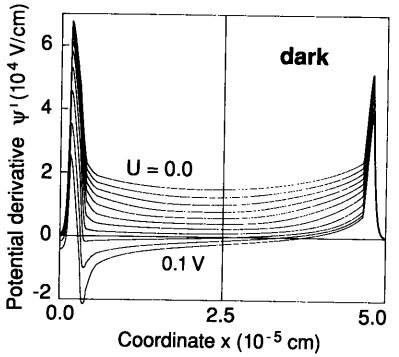

Fig.8 : Ψ'(x) through pin structure

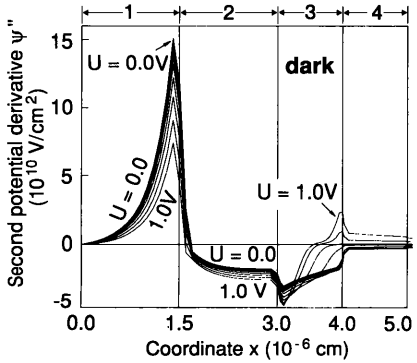

Fig.9 : Ψ''(x) through regions 1 to 4

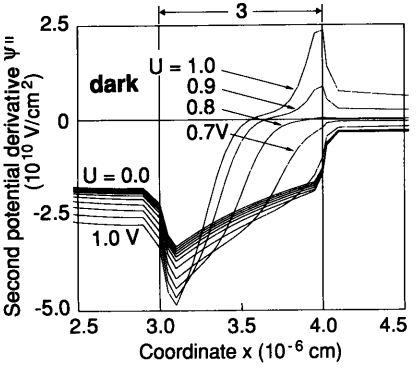

Fig.10 : Ψ''(x) through region 3

uniform buffer section improves the simulated characteristics for instance. A buffer is quite important in any case.

ROOTS OF CHARACTERISTIC EQUATION

A simulation determines the functions ψ, n, p of x by solving the semiconductor equations with boundary conditions. A special algorithm is applied here for that purpose. The regions of Fig.1 are subdivided in as many subregions (zones) as necessary. The equations are linearized in any zone and then form a set of 3 differential equations of second order with constant coefficients and a constant "right side". The homogeneous part of the equations is solved by exponential functions $\exp(\lambda x)$. The relevant reciprocal lengths λ are the roots of an algebraic equation of sixth order (characteristic equation). The local solutions, established by the 6 roots, are put together at the zone boundaries. The inherent nonlinearity of the problem is considered by iteration runs. If the coupling between the equations is switched off, then the roots of 3 quadratic equations fall out that are real altogether. In this degenerate case the roots indicate the Debye length (along and against a permittivity gradient) and diffusion lengths of electron and holes (along and against drift). The appearance of complex roots in the general case points to strong coupling between the semiconductor equations. The 6 roots are numbered λ_1 to λ_6 here to form a rising sequence of their real parts. Fig.11 shows as an example the real functions $\lambda_k(x)$ through the regions 1 to 4 of cell 030 for U = 1.0 V in the dark. The picture is most entangled in region 3.

Fig.12 gives λ_1 for U = 0.1 to 1.0 V. The curves for the lower U-values trace a box through region 3. The curves for the higher U-values penetrate as vertical lines from the right rim into the box, beginning with U = 0.6 V. The vertical line for $U = U_F = 0.75$ V (not shown) would lie amidst the box between the lines for U = 0.7 and U = 0.8 V. Hence the voltages $U_S = 0.55$ V and U_F that limit the blue snake are conspicuous. A part of Fig.11, region 3 alone, is plotted in Fig.13. Where two curves stick together they form a complex pair. The corresponding imaginary parts are not shown. With increasing voltage imaginary parts build up in the dark especially in region 3. It is only for $U > U_F$ that relatively small imaginary parts appear through the whole i-layer.

The roots represent intermediary simulation results. The simulated carrier distributions and characteristics are based on them. Quite a few examples could be presented here only. The

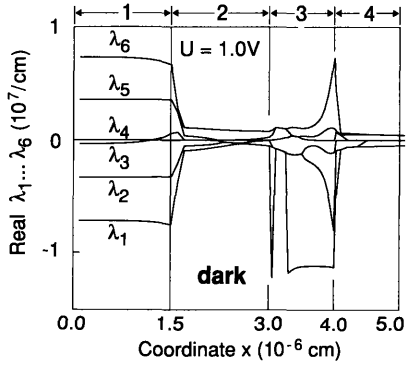

Fig.11 : $\lambda_1(x)$ to $\lambda_6(x)$, U = 1.0 V

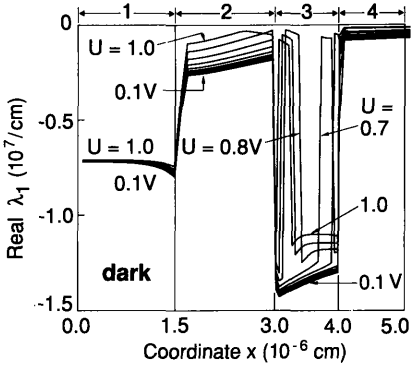

Fig.12 : $\lambda_1(x)$, U = 0.1 to 1.0 V

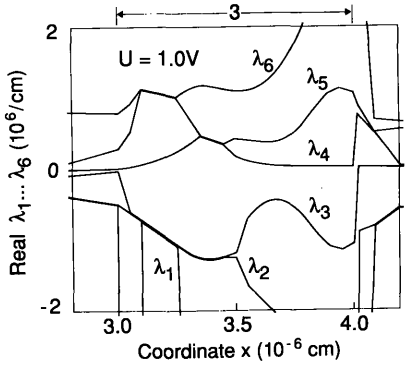

Fig.13 : $\lambda_1(x)$ to $\lambda_6(x)$, U = 1.0 V

progress from analytical modelling to numerical simulation modifies the roots. They contain and express in general the interaction between the semiconductor equations. The specific relations between physical assumptions, roots and cell characteristics have yet to be worked out.

Conclusion

The characteristic roots define exponential functions that convey the space dependence of the potential and of the electron and hole concentrations and currents. The usual simulation techniques (finite differences or elements) don't exploit these roots.

The simulation of pin cells with buffer (by means of characteristic roots as done here or otherwise) leads to special features. Their exemplary elaboration represents the main purpose of this work. An electron inversion layer for example builds up beyond flat bands as a consequence of reduced "surface recombination". The repercussion on space charge and field is demonstrated. The intention here was not to specify the most favorable buffer. The "disturbance" rather introduced with a buffer was presented in a qualitative manner. To realize the best buffer remains a matter of technology. Simulations yield insight and are helpful insofar.

REFERENCES

[1] Y. Tawada et al, Appl.Phys.Lett. **39**(3) 237 (1981)
[2] S.J.Fonash and S.Ashok, Appl.Phys.Lett **35**(7) 535 (1979)
[3] B.Abeles et al, Thin Solid Films **90** 441 (1982)
[4] A.Catalano and G.Wood, Mat.Res. Soc.Symp.Proc. **118** 581 (1988)
[5] H.Sakai et al, **6**th European Photovoltaic Solar Energy Conf. London, 682 (1985)
[6] R.R.Arya et al, Int'l PVSEC-**3**, Tokyo, 457 (1987)
[7] M.Hack et al, IEEE-ED **36** 2764 (1989)
[8] I.Sakata and Y.Hayashi, Appl.Phys. **A37** 153 (1985)
[9] H.Pfleiderer et al, **20**th IEEE PVSC 180 (1988)
[10] M.B. von der Linden et al, **11**th European Photovoltaic Solar Energy Conf. Montreux, 647 (1992)
[11] W.J.Kopetzky et al, Journal of Non-Crystalline Solids **137&138** 1201 (1991)
[12] F.Smole and J.Furlan, J.Appl.Phys. **72** 5964 (1992)